



3D live imaging and phenotyping of CAR-T cell mediated-cytotoxicity using high-throughput Bessel oblique plane microscopy

Received: 1 April 2024

Accepted: 29 July 2024

Published online: 06 August 2024

 Check for updates

Zhaofei Wang^{1,5}, Jie Wang^{1,5}, Yuxuan Zhao^{1,5}, Jin Jin^{2,5}, Wentian Si¹, Longbiao Chen¹, Man Zhang², Yao Zhou¹, Shiqi Mao¹, Chunhong Zheng³, Yicheng Zhang², Liting Chen²  & Peng Fei^{1,2,4} 

Clarification of the cytotoxic function of T cells is crucial for understanding human immune responses and immunotherapy procedures. Here, we report a high-throughput Bessel oblique plane microscopy (HBOPM) platform capable of 3D live imaging and phenotyping of chimeric antigen receptor (CAR)-modified T-cell cytotoxicity against cancer cells. The HBOPM platform has the following characteristics: an isotropic subcellular resolution of 320 nm, large-scale scouting over 400 interacting cell pairs, long-term observation across 5 hours, and quantitative analysis of the Terabyte-scale 3D, multichannel, time-lapse image datasets. Using this advanced microscopy platform, several key subcellular events in CAR-T cells are captured and comprehensively analyzed; these events include the instantaneous formation of immune synapses and the sustained changes in the microtubing morphology. Furthermore, we identify the actin retrograde flow speed, the actin depletion coefficient, the microtubule polarization and the contact area of the CAR-T/target cell conjugates as essential parameters strongly correlated with CAR-T-cell cytotoxic function. Our approach will be useful for establishing criteria for quantifying T-cell function in individual patients for all T-cell-based immunotherapies.

Immunotherapy has undoubtedly revolutionized cancer treatment^{1–4}. For instance, chimeric antigen receptor (CAR)⁵-engineered T cells (CAR-T cells) have ushered in a new era for treating hematological malignancies. However, highly selected patients still have overall response rates (ORRs) ranging from 50–90%⁶. Furthermore, only a small proportion of patients achieve long-term remission from immunotherapy⁷. Visualization and analysis of the cytotoxic process of CAR-T cells, which typically involves recognizing and killing target cells, can be accomplished through fluorescence microscopy. This approach thus has the potential to predict the efficacy of T-cell-based cellular immunotherapy⁸. However, current functional studies of CAR-

T cells have focused mostly on the typical attributes of cell populations and lack long-term phenotyping of antitumor cytotoxicity at the subcellular level; the latter has great potential for the identification of the efficacy-related biomarkers.

In contrast to classical fluorescence microscopy techniques, light-sheet fluorescence microscopy (LSFM) can rapidly image live cells in three dimensions (3D) with low phototoxicity, thereby allowing for a more physiologically relevant assessment of T-cell functionality⁸. The LSFM not only intuitively reveals the dynamic physiological processes of cell toxicity^{9–11} but also facilitates the regression analysis of the cell states through the feature analysis of

¹School of Optical and Electronic Information-Wuhan National Laboratory for Optoelectronics, Huazhong University of Science and Technology, Wuhan 430074, China. ²Department of Hematology, Tongji Hospital, Tongji Medical College, Huazhong University of Science and Technology, Wuhan, China.

³International Cancer Institute, Peking University Cancer Hospital and Institute, Peking University, Beijing, China. ⁴Advanced Biomedical Imaging Facility, Huazhong University of Science and Technology, Wuhan, Hubei 430074, China. ⁵These authors contributed equally: Zhaofei Wang, Jie Wang, Yuxuan Zhao, Jin Jin. ✉ e-mail: ltchen@tjh.tjmu.edu.cn; feipeng@hust.edu.cn

the images¹². However, due to the absence of an efficient sample mounting and data analysis pipelines, current LSM techniques are regarded as low-throughput imaging techniques limited to the observation and analysis of individual cells¹² and cannot be used to study large-scale cell events at high throughput. Due to the heterogeneity of CAR-T cells^{13,14}, the results from the analysis of the individual cells potentially exhibit significant discrepancies in overall performance. Therefore, a high-throughput long-term live-cell imaging system is needed for analyzing the CAR-T-cell cytotoxicity.

Previous studies based on 2D microscopy reported that the quality of the CAR-mediated immunological synapse (IS) was essential for CAR-T cell cytotoxicity^{15–18}. Although 3D microscopy allows for comprehensive observation of IS formation, the lack of automated data analysis methods limits the throughput of analyses¹⁹. As an exploration of analytical methods, deep-learning-based approach has recently accomplished segmentation of 3D IS²⁰. However, the training data dependency makes it difficult to analyze complicated IS morphological features.

In this study, we develop a high-throughput, high-resolution, multidimensional live-cell phenotyping pipeline consisting of the following: a dedicated microfluidic chip for large-scale pairing of the CAR-T/tumor cells; a high-throughput Bessel oblique plane microscopy (HBOPM) that could automatically detect immune cytotoxicity events and three-dimensionally image the subcellular interactions at high spatiotemporal resolution over a long tumor killing time of hours; and a comprehensive spatial-spectrum cell phenotyping algorithm that could specifically identify and quantitatively analyze organelle phenotypes that are strongly correlated with the killing efficacy. With this microfluidics-enabled intelligent HBOPM platform, we reveal the dynamics of immune synapses as key factors for evaluating the cytotoxicity of CAR-T cells.

Results

Overview of high-throughput Bessel oblique plane microscopy (HBOPM)

We designed an open-environment microchamber chip containing 2000 cylindrical chambers (50- μm diameter \times 50- μm depth) to accommodate the CD3 + T cells transduced with concentrated CAR19-Lifeact-EGFP lentivirus and Nalm6 tumor cells with membranes labeled with mApple (Fig. 1a). The CAR-T and Nalm6 cells were mixed 1:1 on the chip to form large CAR-T-Nalm6 cell pairs in the microchambers (Fig. 1b, Supplementary Fig. 1). Notably, we fabricated the microchip using Bio-133 glue, a material with a water-like refractive index of 1.33, to ensure imaging without aberration from the microchambers²¹. We devised a smart imaging algorithm based on automatic image scoring to enable instant positioning of the preferred microchambers, where CAR-T cells were paired with tumor cells one on one (Fig. 1c, Supplementary Fig. 2).

To three-dimensionally image the large-scale antitumor cytotoxic effects of these cell pairs, we developed a Bessel OPM (Fig. 1c, Supplementary Fig. 3) by combining the OPM setup^{22–26} with double-ring Bessel light-sheet illumination²⁷ (Fig. 1d). OPM setting enables on-chip light-sheet excitation/detection from the same objective, improving system usability. Meanwhile, the enhanced double-ring Bessel light-sheet leverages the interference effect of the double-ring to suppress the sidelobes of the single-ring Bessel light-sheet^{27–29}, providing an extended illumination length and sharp optical sectioning suited for imaging floating CAR-T cells (Fig. 1e). Target cells and CAR-T cells were loaded on one chip in sequence, and this intelligent HBOPM rapidly identified 40 qualified wells and recorded their entire 3D timelapse cytotoxic events. We designed an axial-to-lateral isotropic deep learning network (Supplementary Fig. 4) to reconstruct the light-sheet image sequence of cell interactions with a 3D isotropic resolution of ~ 320 nm (Fig. 1f) and low phototoxicity for over 700 measurements; these were both superior to line-confocal microscopy (compared in Fig. 1g).

We also developed a phenotype analysis pipeline for automatically processing these terabyte images with high throughput (Fig. 1h, Supplementary Figs. 5–7). This pipeline could automatically extract the numerical features from the cells for analysis, thereby evaluating the cytotoxic activities through quantifying CAR-T actin's motion, their contact areas with the tumor cells and the polarity of the microtubule organizing center (MTOC). The workflow of HBOPM is shown in Supplementary Movie 1.

Smart imaging algorithms and imaging strategies

In the smart imaging procedure (Fig. 2a, Supplementary Movie 2), we used bright-field mode to quickly obtain images of the chip (Fig. 2a) and then used the template matching algorithm to discern the coordinates of all the microchambers (Fig. 2b). Furthermore, in wide-field fluorescence mode (Fig. 2c), we detected chambers with the desired cell pairs (Fig. 2d) by deep learning segmentation and scoring algorithms (Fig. 2e–h). We segmented the bright-field fluorescence composite image into small blocks based on the localization results (Fig. 2e) and then used CellPose³⁰ deep learning segmentation to identify the cells in each microchamber (Fig. 2f). Based on the above segmentation results, we could quantify the cell distribution in each microchamber. As shown in Fig. 2g, cell A and cell B, which had fluorescence signals, were recognized as CAR-T cells and tumor cells, respectively, while the remaining cells without fluorescence were considered T cells that were not engineered with the CAR gene. When the number of CAR-T cells or tumor cells in the microchamber was not equal to 1, the microchamber score was set to zero. Otherwise, we scored the chamber based on the fluorescence intensity of the CAR-T cells. Thus, we obtained a scoring table for all microchambers (Fig. 2h). Finally, the coordinates of the selected microchambers were returned to the control software for light-sheet imaging (Fig. 2i) in continuous or long-term mode.

To capture both the cellular motion details and long-term features, we applied continuous imaging for 15 minutes and long-term imaging for 5 hours. Using a continuous imaging strategy (CIS, Fig. 2k), we three-dimensionally imaged the interactions of the paired CAR-T cells/target cells in each chamber at a rate of 0.4 volume/s for 15 minutes. Under a long-term imaging strategy (LIS Fig. 2l), we also captured the images at a rate of 0.4 volume/s for 15 s each round and then switched to the next cell. After 40 chosen cells were imaged, they were returned to the first cell, and the above process was repeated, with each imaging cycle lasting 10 minutes (15 s/cell \times 40 cells). LIS not only improved the imaging throughput but also notably reduced the phototoxicity to cells, extending the imaging window of CAR-T cells from a few minutes³¹ to several hours until the endpoint was reached. The combination of CIS and LIS thereby established cross-validation for compressive visualization of the cytotoxic activities.

Imaging of the CAR-T/Nalm6 immune synapse (IS) formation

The immune synapse is known to play a crucial role in the cytotoxicity of both the T-cells and CAR-T cells^{16–18,32}. With intelligent HBOPM imaging, we first performed high-throughput 3D timelapse imaging of early immune synapse (IS) formation in real CAR-T/Nalm6 interactions. Previous studies suggested that when T cells formed immune synapses, they usually contacted the target cells on the dense actin side, followed by the polarized movement of the MTOC toward the target cells⁹; however, based on our results (Fig. 3a, Supplementary Movie 3), the CAR-T cells tended to establish immune synapses on the MTOC side, usually on the sparse actin side. Subsequently, instead of MTOC, actin polarized toward the target cell, aggregated around the target cell to form the IS, and ultimately completed the cytotoxicity process (Fig. 3b–f). Interestingly, when CAR-T cells were treated with dasatinib³³, a drug reported to induce a function-off state in CAR-T cells, their cytotoxicity appeared to be

blocked at the contact state, as shown in Fig. 3b–f. These CAR-T cells tended to contact and adsorb to the tumor cells on the MTOC or sparse actin side, but the actin polarity reversal and an effective IS formation was suppressed. (Fig. 3g, Supplementary Movie 4). Through CIS, we recorded the actual process of actin polarity reversal when the CAR-T cells formed immune synapses (Fig. 3h, Supplementary Movie 5). We observed that 62.8% of the cells followed the pattern shown in Fig. 3h, and 28.2% of the cells did not undergo significant polarization before forming immune synapses. Only 9% of the cells formed immune synapses on the dense actin side, after which the MTOC migrated (Supplementary Fig. 8). These results provide insights into CAR-T/target cell IS formation.

Cytotoxicity analysis algorithms (CAAs)

To analyze a large amount of multi-channel 3D timelapse image data, we developed a CAAs for the automatic quantification of the cell features (Fig. 4). The raw light-sheet imaging data were initially subjected to the reconstruction algorithm (RA) to restore the spatial relationship of the OPM (Fig. 4a, b); then, the 3D timelapse image data were subjected to a quantitative algorithm (QA) to obtain the quantitative indicators of the cells (Fig. 4c–g). Based on previous reports, we selected 5 QA indicators to quantify the characteristics of the CAR-T cells, including the area of the IS, actin retrograde flow speed, actin depletion coefficient of the IS, MTOC polarization angle, and tumor cell death rate. The tumor cell death rates could be directly

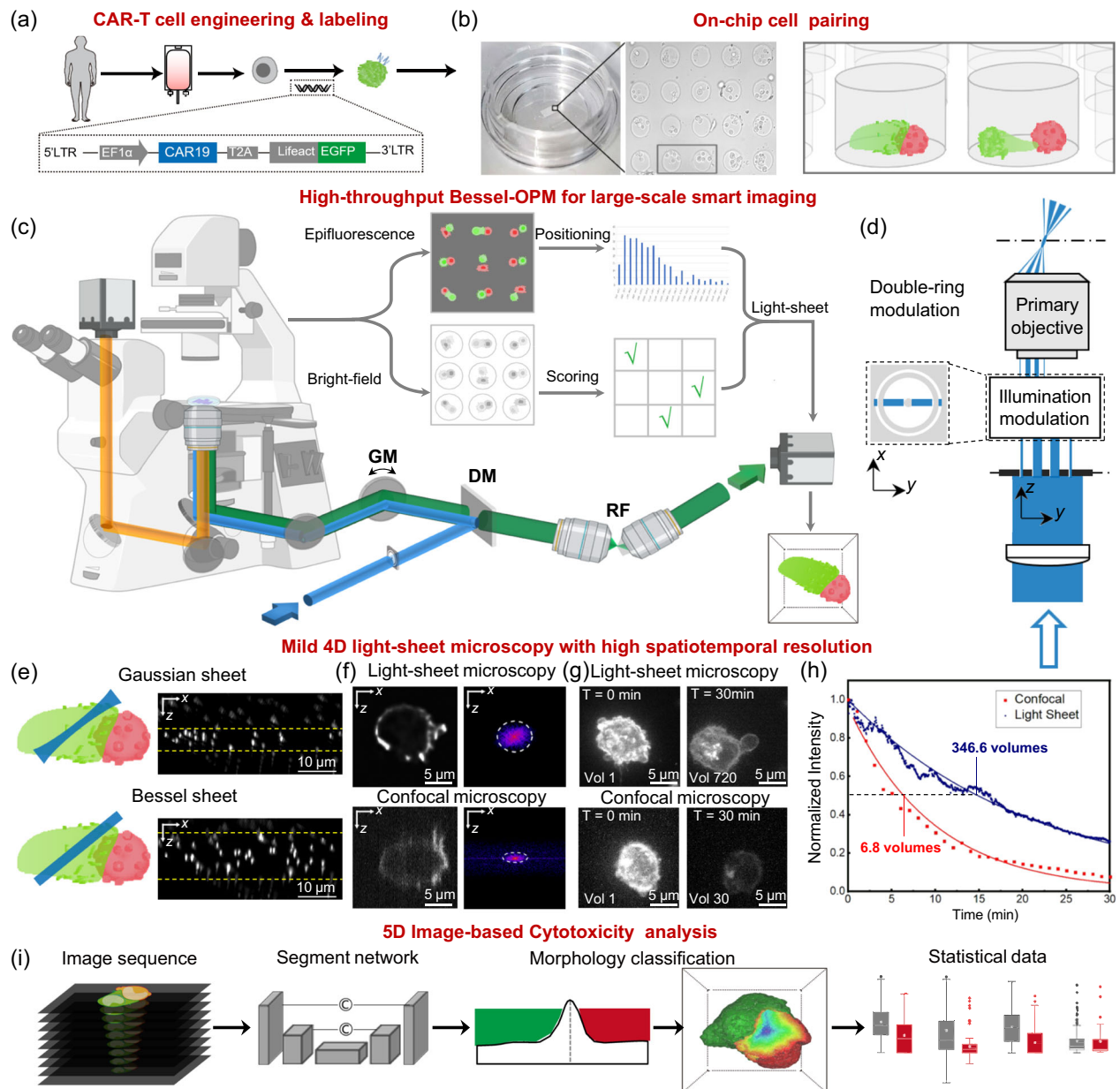


Fig. 1 | Setup of the high-throughput Bessel oblique plane microscopy (HBOPM). **a** Cell engineering to prepare CAR-T cells transfected with the CAR19 and EGFP genes. **b** Microchamber chip structure diagram. The cells were loaded into the chip. **c** HBOPM composed of smart imaging algorithms, the Bessel-OPM optical system and cytotoxicity analysis algorithms. GM galvo mirror, DM dichroic mirror, RF remote focus system. **d** Double-ring modulation to generate ultrathin Bessel light-sheets with tunable axial extents from 0.5 to 1.5 μm . **e** Comparison between Gaussian and Bessel light-sheets. **f** Comparison of axial resolution between

the confocal microscope and our HBOPM. The HBOPM images were processed by our super-resolution network. Fluorescence images are presented on the left, while Fourier transforms of the images are shown on the right. **g** Comparison of photobleaching between confocal microscopy and our system. **h** Quantitative analysis of the photobleaching rate. The fitted curves (solid lines) indicate exponential decays with half decays at -7 and -347 volumes for confocal and HBOPM, respectively. **i** Cell phenotype analysis pipeline containing the image reconstruction, segmentation, identification and analysis.

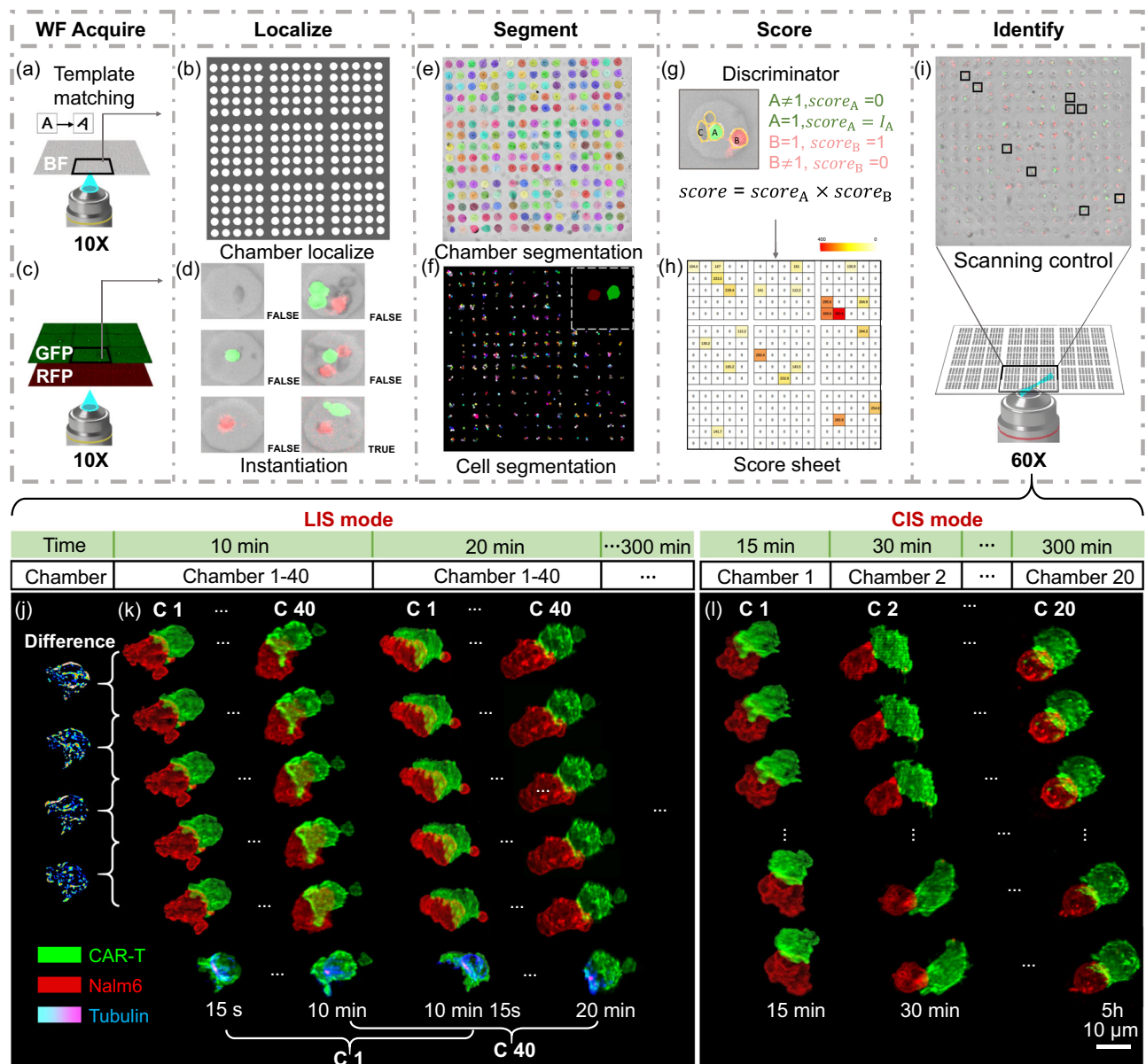


Fig. 2 | Smart imaging procedure and imaging strategy. **a–i** Smart imaging procedure. **a** BF mode with a 10 \times objective. **b** Localization of all microchambers based on wide-field images using the smart imaging algorithms. **c** Wide-field fluorescence mode with a 10 \times objective. **d** Example of evaluation criteria. “TRUE” indicates a qualified chamber. **e** Chamber segmentation. **f** Segmentation of all cells via deep learning. **e, f** could represent 117 independent experiments. **g** Scoring criteria. **h** Score table of each chamber. **i** Identification of the chambers with highest scores. The microscope was switched to OPM mode. **j–i** Continuous and long-term

imaging strategy (CIS & LIS). **j** Differences between the adjacent volumes. **k** LIS mode. The algorithm automatically selected 40 microchambers, completed a scan round within 10 minutes, and imaged 6 volumes in 15 s per microchamber. The first five volumes contained three-channel information on CAR-T-cell actin, Nalm6 cell membranes and SYTOX blue, while the last volume contained CAR-T-cell actin and CAR-T-cell tubulin. **l** CIS mode. The algorithm selected several microchambers and continuously imaged each for 15 minutes. All volumes contained three-channel information on CAR-T-cell actin, Nalm6 cell membranes and SYTOX blue.

determined based on SYTOX BLUE staining (Fig. 4c, Supplementary Movie 6), while the remaining indicators required algorithms to extract the information from the images.

Prior research on IS has focused primarily on the 2D IS formed by the T cells on the surface of antigen-coated slides^{18,34,35}. The QA introduces a contact surface segmentation algorithm (CSSA), which can accurately segment the 3D contact surface with a thickness of 1 pixel, and the area of the interactive IS can then be obtained (Fig. 4d, Supplementary Fig. 7). Furthermore, we developed an iterative erosion algorithm (IEA) to obtain the distance from every segmented pixel on the IS to its center and calculated the actin depletion coefficient r between this distance and the corresponding fluorescence signal intensity of F-actin (Fig. 4e, Supplementary Fig. 7).

In both cytotoxic T lymphocytes (CTLs) and natural killer (NK) cells, robust actin polymerization-driven retrograde actin flow at the perimeter of the IS was observed^{36,37}. However, whether the actin retrograde flow occurred in CAR-T cells and its role in the effectiveness of CAR-T cells were not clear^{9,12}. In QA, we defined the vector pointing from the center of the IS to the center of the CAR-T-cell as the axis of interaction (AOI), identified and tracked the dendritic actin structures on the T-cell surface, recorded the displacement vectors (Fig. 4f) of these structures within the 15 s imaging window, and statistically measured the intensity of the projection of these displacement vectors onto the AOI vector to extract the eigenvalues of actin flow during this period. We also calculated the angle between the AOI and the vector from the MTOC to the center of the CAR-T cells (Fig. 4g), which was

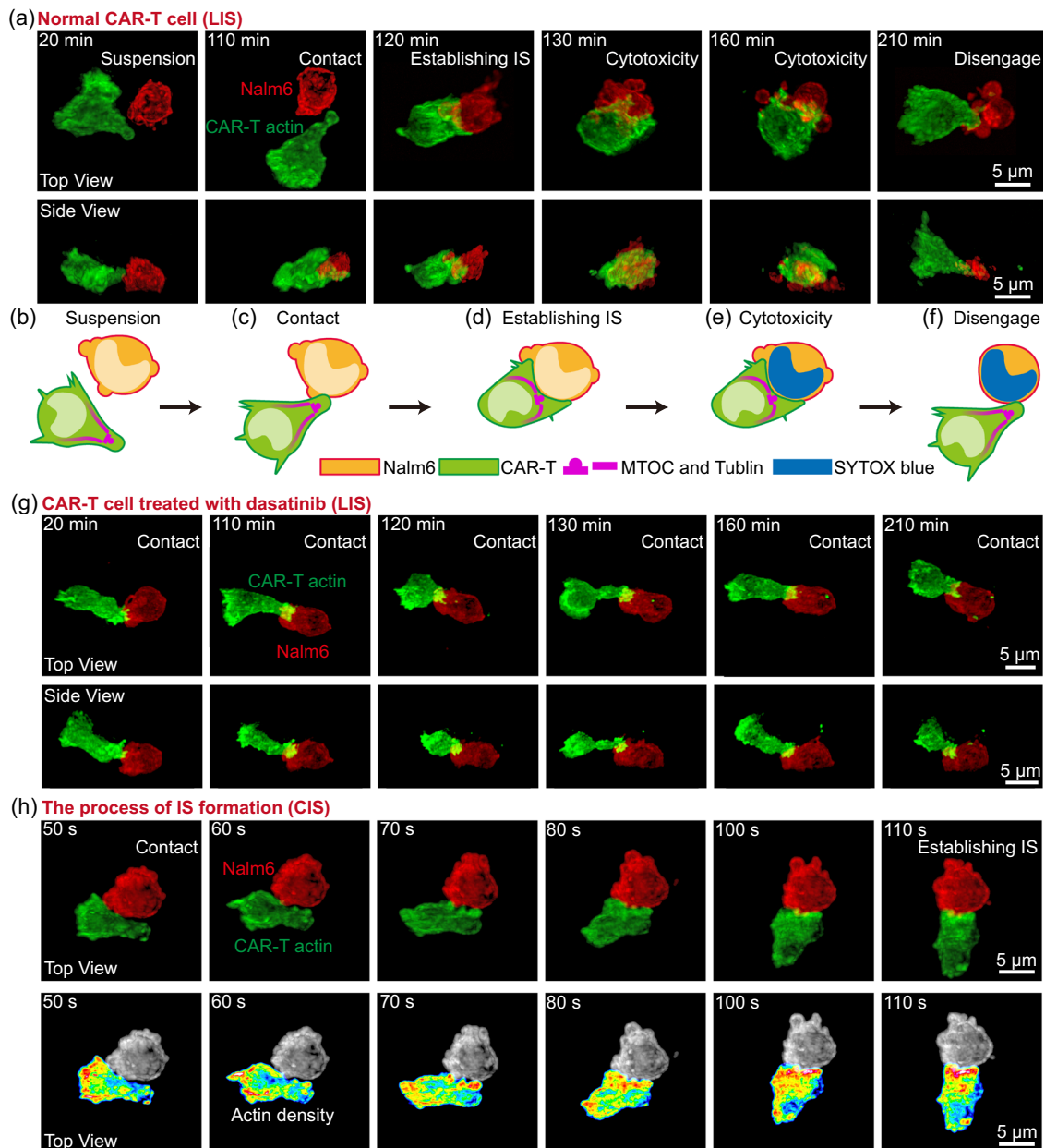


Fig. 3 | Cytotoxic behavior. **a** A normal CAR-T-cell captured by the HBOPM under a long-term imaging strategy (LIS). The upper column is the top view of the 3D image, and the lower column is the side view. Figure could represent 49 independent samples. **b–f** Schematic diagram of a typical cytotoxic behavior pattern. **b** During the separation stage, some CRA-T cells undergo morphological polarization. **c** Polarized CRA-T cells tend to contact the target cells with sparse actin. **d** Actin density polarity undergoes reversal, and IS is established. **e** Cytotoxic process

killing target cells. **f** CAR-T cell polarity restoration and attempt to disengage from target cells. **g** CAR-T cells treated with dasatinib captured by HBOPM under LIS. Its cytotoxic behavior was blocked at the contact stage. Figure could represent 55 independent samples. **h** Normal CAR-T-cell captured by the HBOPM under a continuous imaging strategy (CIS). The above column displays the original fluorescence image, while the following column uses a heatmap to illustrate the change in the polarity of the actin density. Figure could represent 5 independent samples.

termed the MTOC polarization angle, to investigate the reorientation of the MTOC during the cytotoxic process³⁸.

Quantitative analysis using the CAAs

Figure 5a (Supplementary Figs. 9, 10) shows the actin retrograde flow speed of the CAR-T cells from Fig. 3a. A correlation was observed between the flow speed and the cytotoxicity stage. Figure 5b shows the visualization of the actin movement traces at the peak flow speed in the state of established IS; these results indicated that actin tended to flow in the opposite direction of the immune synapses.

Using the CAAs, we analyzed all data. We imaged CAR-T cells from 10 healthy donors to determine the baseline. Three of the ten donor-

derived CAR-T cells were also imaged after treatment with dasatinib to test the sensitivity of specific indicators to CAR-T-cell function. Figure 5c–e (Supplementary Fig. 11) shows the statistical results from the area of IS, the actin depletion coefficient of IS and the actin retrograde flow speed, and all three statistical indicators showed a significant decrease in dasatinib-treated cells. The MTOC polarization angle showed a distribution trend of less than 90 degrees, but no significant difference was observed in this indicator between the dasatinib-treated CAR-T cells and the controls (Fig. 5f, Supplementary Figs. 12, 13); these results indicated that dasatinib might not block the physiological process of MTOC polarization. Moreover, the tumor cell death rates were also significantly reduced in the dasatinib-treated

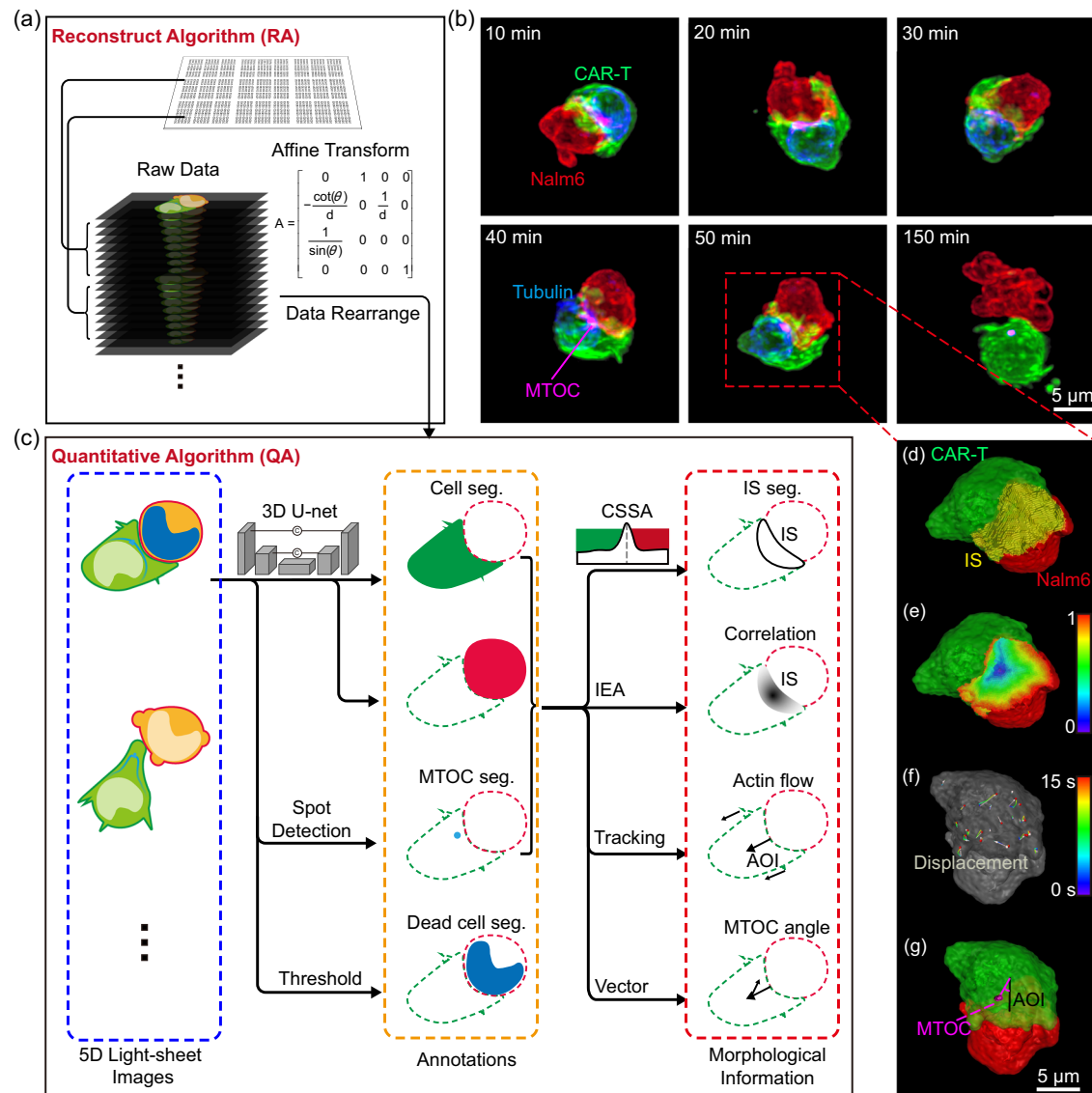


Fig. 4 | Cytotoxicity analysis algorithms (CAAs). **a** Reconstruct algorithm (RA). The raw image data captured by the HBOPM required data rearrangement and affine transform batch processing to calibrate the tilted spatial relationship of the HBOPM. **b** Reconstructed 3D timelapse image data. **c** QA Quantitative algorithm, contact surface segmentation algorithm CSSA, iterative corrosion algorithms IEA.

d–g Visualization of intermediate results in QA. **d** The segmentation of the immune synapses by CSSA. **e** Normalized edge distance of the immune synapses via the IEA. **f** Actin flow trace via a tracking algorithm. **g** Visualization of the MTOC polarization angle. Panels **b**, **d**, **e** could represent 419 independent samples.

cells (Fig. 5g). We merged data from different sources of healthy donors to obtain a distribution box chart for the four indicators mentioned above, with the exception of the tumor cell death rates, to visually demonstrate the above conclusions.

Discussion

In summary, based on the development of intelligent HBOPM and T-cell behavior analysis, we accomplished high-throughput, long-term 3D imaging and phenotyping of CAR-T/Nalm6 interactions to comprehensively analyze the antitumor cytotoxic function of CAR-T cells. The advanced imaging technique in conjunction with high-dimensional image-based analysis formed an automated and scalable cell observation and analysis pipeline well suited for diverse types of cell research. In our study, we tested the ability of this system to evaluate the function of CAR-T cells in specific cases. The visualization and statistical results were significantly different between the dasatinib-treated CAR-T cells and controls, validating the effectiveness of our platform.

In our HBOPM experiments, we used two temporal sampling modes, LIS and CIS. LIS allows for imaging cells with higher throughput and lower phototoxicity, making it well suited for observing regular events, such as cytotoxicity process, in large cell populations over long period. Meanwhile, CIS offers good temporal resolution for continuously observing fast subcellular events, such as the formation of immune synapses. It is noteworthy that HBOPM can provide more imaging options, with adjustable temporal resolution and throughput according to specific applications. There is also potential for our smart imaging algorithms to detect cellular events³⁹ by adding an image classifier like VGG⁴⁰. Our algorithms were based on machine vision algorithms and utilized prior information on the position distribution of microchamber chips. Through simplifying the target detection problem into an image classification problem, our algorithm can potentially reduce the reliance on training data and enhance the detection efficiency. On the other hand, improving HBOPM from the perspective of microfluidics is also promising. Enhancing cell pairing efficiency using microfluidic advancement could facilitate wide-field

imaging at low magnification, thereby further improving the imaging and analysis throughput of the system. In addition, microfluidics can be used to control drug concentration gradients in different microchambers⁴¹, thereby facilitating the assessment of drug efficacy.

In addition to these potentials, our HBOPM still has other limitations. Thirty minutes are required for the cells to mix and initiate imaging. Capturing the early events of the immune synapse formation on a larger scale still requires further optimization. Moreover, the

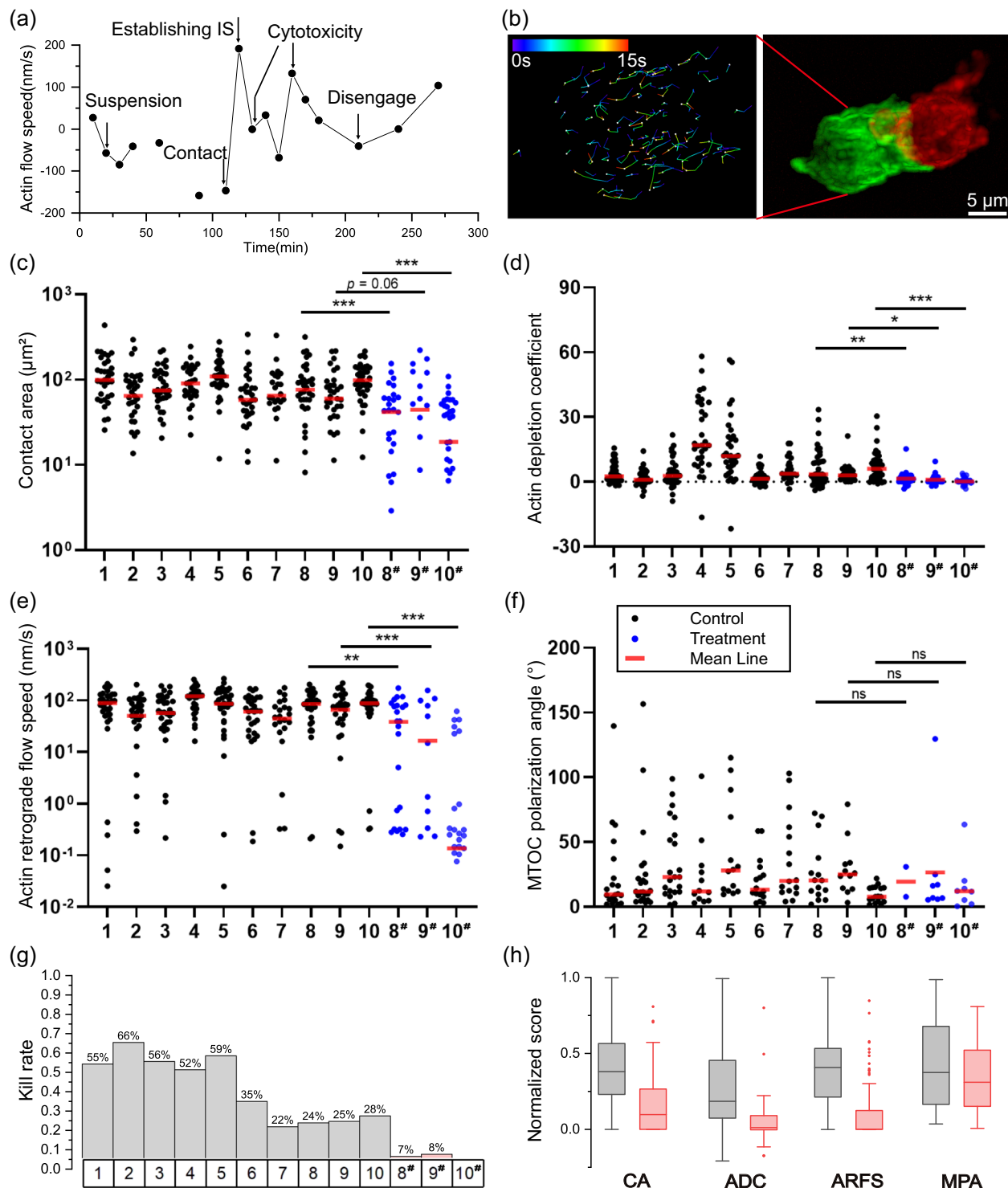


Fig. 5 | Cytotoxicity quantitative statistical analysis. **a** Use of the algorithm to quantify the actin flow velocity shown in Fig. 3a. **b** Actin flow traces at 120 minutes. **c–f** Points indicate a single CAR-T cell and p -value was performed using one-way ANOVA analysis. **c** Graph of the IS area. We collected 419 biologically independent samples in 13 high-throughput experiments ($n = 419$). **d** Graph of the actin depletion coefficient between the normalized edge distance and actin fluorescence intensity. $n = 419$. **e** Graph of actin flow speed. $n = 419$. **f** Graph of the MTOC bias

angle. $n = 185$. **g** Graph of the mortality rate of Nalm6 cells labeled with SYTOX blue. **h** Summary graphs of the data from **c–f**, where the cells treated with dasatinib are red and the control cells are gray. Boxes indicate 25–75% of data, whiskers indicate outlier and lines indicate the median. n values for each column are 419, 419, 419 and 185. #: dasatinib-treated group, * $p < 0.05$, ** $p < 0.01$, *** $p < 0.001$, ns no-significance. Source data and exact p values are provided as a Source Data file.

optimization of the analysis algorithm is insufficient, leaving room for improvement in the 8-hour running time.

Our method has broad research prospects. Quantifying cellular behavior from multi-channel 3D timelapse images has plenty of possibilities. Therefore, we envision that more quantitative algorithms can be utilized for information mining of the image data. For example, in our result, we found that there may be errors in using dyes (SYTOX™ Blue or PI) to indicate whether target cells were killed. The apoptosis of target cells often starts with the morphological changes. Some cells expand and become round, some cells break into pieces, and dead and live dyes usually need to be delayed for several hours to cause the emission of fluorescence from the dead target cells. In our study, the death time of the target cells was not calculated, but the death time of the target cells determined from a morphological perspective may have research value. In addition, many other phenomena, such as microtubule morphology distribution and the CAR-T-cell length-to-diameter ratio, could be statistically analyzed. From a cellular physiological perspective, why do CAR-T cells tend to form immune synapses on the centrosome side? Is this related to receptor distribution? Our study focused on the methods, and we have not yet conducted in-depth research on the abovementioned aspects.

Notably, all killer cell-based immunotherapies should have the potential to use our platform for an in-depth study of the microscopic behaviors of cells. Since the IS contact area and actin flow speed were identified as the key markers strongly related to the killing efficacy of CAR-T cells, we anticipate that our approach can effectively advance cancer immunotherapy and support clinical trials in the future.

Methods

This study was approved by the medical ethics committee of Tongji Hospital, Tongji Medical College, Huazhong University of Science and Technology (TJ-IRB202303138).

Cell lines and cell culture

The acute B-lymphocytic leukemia cell line Nalm6 (catalog No. CRL-3273) was cultured in RPMI 1640 medium (Gibco, Grand Island, NY, USA) supplemented with 10% fetal bovine serum (FBS; Gibco, Grand Island, NY, USA). The lentivirus packaging cell line LentiX™293 T (catalog No. CRL-3216) was cultured in Dulbecco's modified Eagle medium (DMEM) (Gibco, Grand Island, NY, USA) supplemented with 10% FBS. The strains were obtained from the American Type Culture Collection (ATCC) and authenticated by short tandem repeat (STR) analysis before use. All cells were tested and confirmed to be negative for mycoplasma.

Recombinant plasmid construction and lentivirus packaging

The anti-CD19 scFv (single-chain variable fragment) was grafted into a second-generation CAR with a CD8a hinge/transmembrane region, a CD28 costimulatory domain, and an intracellular CD3 ζ . The scFvs were derived from the FMC63 clone under patent WO2012079000⁴². Then, the CD19 CAR gene was linked to Lifeact-EGFP⁹ via the T2A sequence to facilitate *in vitro* visualization. mTagRFP-Membrane-1 was a gift from Michael Davidson (Addgene plasmid # 57992), and we replaced mTagRFP with mApple to construct the mApple-Mem plasmid. Recombinant plasmids were extracted by using the EndoFree Plasmid Maxi Kit (Qiagen, Hilden, Germany) according to the manufacturer's instructions. Lenti-X™293 T cells were co-transfected with a vector carrying the target gene (CD19 CAR-Lifeact-EGFP or mApple-Mem) and the psPAX2 and PMD2.G packaging plasmids using the transfection agent Lipofectamine 3000 (Invitrogen, Waltham, MA, USA). The viral supernatants were collected, filtered, and concentrated 48 hours after transfection by ultracentrifugation (Avanti J-26S XPI) and then aliquoted and stored at -80°C .

Isolation, activation, transduction and culture of T cells

Peripheral blood mononuclear cells from 10 healthy donors (HDs) were purchased from Milestone® Biotechnologies, China. Peripheral blood mononuclear cells (PBMCs) were isolated by density gradient centrifugation on Ficoll-Paque Plus (GE Healthcare, Boston, MA, USA). CD3+ T cells from PBMCs were separated using CD3 microbeads (Miltenyi Biotec, Bergisch Gladbach, Germany) following the manufacturer's instructions. Then, the T cells were stimulated with Dynabeads™ Human T-Activator CD3/CD28 (Gibco, Grand Island, NY, USA) at a 1:1 ratio in CTS™ OpTmizer™ medium (Gibco, Grand Island, NY, USA) containing 5% human AB serum, 2 mM l-glutamine (Gibco, Grand Island, NY, USA) and 200 IU/mL rhIL-2 (PeproTech, Rocky Hill, NJ, USA). Within 24 hours, primary T cells were transduced with concentrated lentivirus at a certain multiplicity of infection (MOI) ranging from 2 to 5. Twenty-four hours later, the T cells were centrifuged and resuspended in fresh culture medium at a density of $1-2 \times 10^6/\text{mL}$. Imaging and functional assays were performed after 12 days of culture *in vitro*.

Construction of mApple-Mem-expressing Nalm6 cell lines

Nalm6 cells were transduced with concentrated mApple-Mem lentivirus at a certain MOI in the range of 30 to 50 for 4 hours. mApple-positive cells were sorted 5 days after infection on a Moflo XDP flow cytometer (Beckman Coulter) to obtain mApple-Mem-expressing Nalm6 cell lines.

Cell preparation for imaging

For experiments on the impacts of dasatinib, CAR-T cells were pre-treated with 50 nM dasatinib (Selleck, Shanghai, China) for 24 hours. Due to the reversible effect of dasatinib, 50 nM dasatinib was also added to all subsequent staining, imaging, and other experimental solutions.

To label the microtubules, CAR-T cells were stained with a SiR-tubulin probe (SpiroChrome, Switzerland) to a final concentration of 2 μM and incubated for 1 hour in a humidified 5% CO₂ incubator at 37 $^{\circ}\text{C}$ ⁴³. The cells were then washed twice with warm phosphate buffer saline (PBS) and resuspended in an imaging solution consisting of phenol red-free 1640 medium (Gibco, Grand Island, NY, USA) supplemented with 10% FBS, 25 mM N-2-hydroxy-ethylpiperazine-N'-2-ethanesulfonic acid (HEPES, Gibco, Grand Island, NY, USA), 100 U/mL penicillin and streptomycin (Gibco, Grand Island, NY, USA), and 1 μM SYTOX™ Blue stain (Invitrogen, Waltham, MA, USA).

Microchip preparation

The first step was to make the mold plate. We designed and customized a polyester mask (SI Fig. 2). Then, we used a photoresist (SU8-2050, Kayaku Advanced Materials) to spin-coat a 50 μm thin layer on a 2-inch wafer and used a UV exposure machine (SUSS MicroTec MA/BAS) to transfer the pattern on the polyester mask to the photoresist; this was developed and used as the mold plate.

The second step was to reverse the mold. The UV-curable adhesive (Bio-133, MyPolymers) was added dropwise onto the mold plate, and the top was flattened as much as possible using a coverslip. After sufficient UV exposure, the cured chip was carefully removed, and the demolded chip was immersed in anhydrous ethanol for more than 24 hours to remove the residual adhesive⁴⁴. The chip was placed at the bottom of a confocal Petri dish and pressed to fix it. Before use, the chip was immersed in sterile water for more than 12 hours to expel the gas inside the chamber, and the use of a vacuum pump to create a low-pressure environment could accelerate the process.

T-cell medium was used to replace the sterile water, 500 μL of the medium was added to the confocal dish to submerge the chip, and then 60 μL of CAR-T cells was added dropwise at a density of $1 \times 10^6/\text{mL}$. The plate was incubated for 10 minutes to allow the cells to fall into the chamber. Subsequently, an equal amount of target cells was removed,

and the above procedure was repeated. Theoretically, the distribution of cells satisfies the binary Poisson distribution, and λ needed to be set to approximately 1. In actual experiments, the smart imaging algorithms estimated λ , which was convenient for the adjustment of the cell density in real time.

Optical system

We built a single-objective light-sheet imaging system using an Olympus ix83 microscope. The system magnification was 63.3 \times , and the primary objective (O_1) used a 60 \times 1.3NA silicone oil objective (UPLSAPO60XS2, Olympus). O_1 was combined with a 40 \times 0.95NA air objective (O_2) (UPLXAPO40X, Olympus) and a set of relay lenses, and this combination formed a 1.05 \times imaging system, which approximately met perfect imaging conditions. The remote-focusing module consisted of O_2 and a 60 \times 1.0NA solid index objective (custom, Special Optics) placed at a 30° angle. The detector arm used dichroic mirrors to simultaneously image all three fluorescence channels. Wide-field imaging used the microscope's original wide-field optical path.

The illumination light path of the single objective light-sheet was also coupled into the microscope. We used a 4-color laser (Colbolt, 405/488/561/633 nm) for illumination and introduced a double-ring modulation (custom chrome plate) on the Fourier plane to generate the Bessel light-sheet.

We carried a sample motor stage (U-780, Physik Instrumente) and a live cell workstation (STXG-WSKMX3WX-SET, TokaiHit) on the microscope rack.

Double-ring Bessel light sheet simulation

We modelled Fresnel diffraction and simulated the thickness and Rayleigh length of the Bessel light sheet for various double-ring parameters. The range of the outer ring radius was estimated based on the Bessel function, and the inner ring was determined using an ergodic search. The simulation code was implemented in MATLAB 2023a.

Smart imaging algorithms

The algorithms were composed of two parts: target detection and optomechanical control. The target detection algorithm is mainly developed based on MATLAB 2023a. The algorithm uses a three-channel wide-field image as the input and outputs the relative localization of 2025 microchambers and the coordinates of the recommended chambers. To achieve this, first, the brightfield image undergoes two rounds of segmentation using the CellPose network³⁰. We set the cell radius to 15 pixels in the first round and 38 in the second round; these correspond to the cell and microchamber radii, respectively. This procedure directly calls the pretrained model and achieves good results without fine-tuning the network. Then, we utilize a secondary template-matching algorithm to localize each chamber. Based on this localization result, the cell segmentation result at the corresponding position is detected, and the cell type and number are determined based on the signal from the fluorescence channel. With a 1-to-1 ratio, all eligible chambers are sorted according to the brightness of the CAR-T cells to provide the recommended results.

The imaging control algorithm is developed based on LabVIEW 2013, which reads the output of the target detection algorithm from the cache file and automatically sets the imaging parameters according to the preset co-positioning relationship between 10 \times and 60 \times .

Super-resolution algorithm

Our deep learning super-resolution algorithm, developed based on the csbDeep toolkit⁴⁵, was tested on a workstation with an NVIDIA GeForce RTX 4090. A single volume (512 \times 512 \times 380 pixels \times 3chanles) needed approximately 2 minutes to process.

We introduced a deconvolution algorithm for building the training data to improve the network performance. The specific approach was to perform Richardson-Lucy deconvolution on the original data

(denoted as I_o) to obtain the I_d based on the measured PSF; then, we refer to⁴⁵ to train a self-supervised deep learning model to perform isotropic super-resolution on the I_d to obtain I_{iso} . Finally, using the pair of I_o and I_{iso} as the training data, a new network was trained for the super-resolution processing of the data.

Analyzing algorithms

To evaluate the reliability of the algorithm, we designed the following experiment: the same batch of CAR-T cells was divided into two groups: one group was treated with the inhibitor dasatinib to simulate impaired cell function, and the other group was left untreated as a control group. Our algorithm performs image analysis of both the experimental group and control group. We compared the algorithm's results to existing research hypotheses and manual evaluations of the experimental data to test its ability to distinguish normal CAR-T cells from functionally inhibited CAR-T cells.

We developed algorithms based on MATLAB 2023a and the packaged front-end as accessible MATLAB apps. We ran the algorithms on a workstation with two CPUs (Intel Xeon Processor E52699 v4 55 M Cache 2.20 GHz) and one GPU (NVIDIA GeForce RTX 4090). As an example, scanning 40 chambers produces raw data with a size of 1.2 TB, and 8 hours was needed to visualize and analyze the data.

The algorithms consist of three parts. The first is the reconstruction of the original light-sheet microscopy data. The process can be abstracted as an affine transformation of the 3D volume. This process took approximately 3 hours.

The second part is to apply a 3D-U-Net to segment the cell structure. The network uses the code from⁴⁶ with some modifications. The source code is in Python, but we coded a MATLAB interface. We retrained the model, and the 3D manual annotation tool used was ImageJ-Labkit⁴⁷. The training process needed approximately 12 hours, and the prediction of a set of experimental data needed approximately 5 hours.

The third part uses morphology, centroid tracking, and other computer vision algorithms to extract and present image information. This part of the algorithm uses parallelization acceleration and runs on the CPU. Approximately 4 hours was needed to run the first part, but a negligible amount of time was needed to run the second part in parallel with the first part.

Reporting summary

Further information on research design is available in the Nature Portfolio Reporting Summary linked to this article.

Data availability

The raw image datasets with Tb size could be made available upon request to the corresponding author. The remaining data are available within the Article, Supplementary Information. Source data are provided with this paper.

Code availability

The associated codes are available on GitHub at <https://github.com/feilab-hust/CAR-T-analysis> for image analysis and <https://github.com/feilab-hust/CAR-T-collection> for data collection.

References

1. Neelapu, S. S. et al. Axicabtagene Ciloleucl CAR T-Cell Therapy in Refractory Large B-Cell Lymphoma. *N. Engl. J. Med.* **377**, 2531–2544 (2017).
2. June, C. H., O'Connor, R. S., Kawalekar, O. U., Ghassemi, S. & Milone, M. C. CAR T cell immunotherapy for human cancer. *Science* **359**, 1361–1365 (2018).
3. Maude, S. L. et al. Tisagenlecleucl in Children and Young Adults with B-Cell Lymphoblastic Leukemia. *N. Engl. J. Med.* **378**, 439–448 (2018).

4. Fuca, G., Reppel, L., Landoni, E., Savoldo, B. & Dotti, G. Enhancing Chimeric Antigen Receptor T-Cell Efficacy in Solid Tumors. *Clin. Cancer Res.* **26**, 2444–2451 (2020).
5. Baker, D. J., Arany, Z., Baur, J. A., Epstein, J. A. & June, C. H. CAR T therapy beyond cancer: the evolution of a living drug. *Nature* **619**, 707–715 (2023).
6. June, C. H. & Sadelain, M. Chimeric Antigen Receptor Therapy. *N. Engl. J. Med.* **379**, 64–73 (2018).
7. Majzner, R. G. & Mackall, C. L. Clinical lessons learned from the first leg of the CAR T cell journey. *Nat. Med.* **25**, 1341–1355 (2019).
8. Rochussen, A. M., Lippert, A. H. & Griffiths, G. M. Imaging the T-cell receptor: new approaches, new insights. *Curr. Opin. Immunol.* **82**, 102309 (2023).
9. Ritter, A. T. et al. Actin Depletion Initiates Events Leading to Granule Secretion at the Immunological Synapse. *Immunity* **42**, 864–876 (2015).
10. Hu, Y. S., Cang, H. & Lillemeier, B. F. Superresolution imaging reveals nanometer- and micrometer-scale spatial distributions of T-cell receptors in lymph nodes. *Proc. Natl Acad. Sci. USA* **113**, 7201–7206 (2016).
11. Ponjavic, A. et al. Single-Molecule Light-Sheet Imaging of Suspended T Cells. *Biophys. J.* **114**, 2200–2211 (2018).
12. Rosenberg, J., Cao, G., Borja-Prieto, F. & Huang, J. Lattice Light-Sheet Microscopy Multi-dimensional Analyses (LaMDA) of T-Cell Receptor Dynamics Predict T-Cell Signaling States. *Cell Syst.* **10**, 433–444 (2020).
13. Khazen, R. et al. Functional heterogeneity of cytotoxic T cells and tumor resistance to cytotoxic hits limit anti-tumor activity in vivo. *EMBO J.* **40**, e106658 (2021).
14. Cazaux, M. et al. Single-cell imaging of CAR T cell activity in vivo reveals extensive functional and anatomical heterogeneity. *J. Exp. Med.* **216**, 1038–1049 (2019).
15. Roybal, K. T. et al. Computational spatiotemporal analysis identifies WAVE2 and cofilin as joint regulators of costimulation-mediated T cell actin dynamics. *Sci Signal* **9**, rs3 (2016).
16. Davenport, A. J. et al. Chimeric antigen receptor T cells form non-classical and potent immune synapses driving rapid cytotoxicity. *Proc. Natl Acad. Sci. USA* **115**, E2068–E2076 (2018).
17. Mukherjee, M., Mace, E. M., Carisey, A. F., Ahmed, N. & Orange, J. S. Quantitative Imaging Approaches to Study the CAR Immunological Synapse. *Mol. Ther.* **25**, 1757–1768 (2017).
18. Xiong, W. et al. Immunological Synapse Predicts Effectiveness of Chimeric Antigen Receptor Cells. *Mol. Ther.* **26**, 963–975 (2018).
19. Camviel, N. et al. Both APRIL and antibody-fragment-based CAR T cells for myeloma induce BCMA downmodulation by trogocytosis and internalization. *J. Immunother. Cancer* **10**, e005091 (2022).
20. Lee, M. et al. Deep-learning based three-dimensional label-free tracking and analysis of immunological synapses of car-t cells. *Elife* **9**, 1–53 (2020).
21. Han, X. et al. A polymer index-matched to water enables diverse applications in fluorescence microscopy. *Lab Chip* **21**, 1549–1562 (2021).
22. Dunsby, C. Optically sectioned imaging by oblique plane microscopy. *Opt. Express* **16**, 20306–20316 (2008).
23. Yang, B. et al. Epi-illumination SPIM for volumetric imaging with high spatial-temporal resolution. *Nat. Methods* **16**, 501–504 (2019).
24. Sapoznik, E. et al. A versatile oblique plane microscope for large-scale and high-resolution imaging of subcellular dynamics. *Elife* **9**, 1–39 (2020).
25. Bouchard, M. B. et al. Swept confocally-aligned planar excitation (SCAPE) microscopy for high-speed volumetric imaging of behaving organisms. *Nat. Photonics* **9**, 113–119 (2015).
26. Yang, B. et al. DaXi—high-resolution, large imaging volume and multi-view single-objective light-sheet microscopy. *Nat. Methods* **19**, 461–469 (2022).
27. Zhao, Y. et al. Isotropic super-resolution light-sheet microscopy of dynamic intracellular structures at subsecond timescales. *Nat. Methods* **19**, 359–369 (2022).
28. Haouas, M., Chebbi, B. & Golub, I. Extension of the span and optimization of the optical “magic carpet”: generation of a wide quasi-nondiffracting light sheet. *J. Optical Soc. Am. A* **36**, 124 (2019).
29. Antonacci, G., Di Domenico, G., Silvestri, S., DelRe, E. & Ruocco, G. Diffraction-free light droplets for axially-resolved volume imaging. *Sci. Rep.* **7**, 1–6 (2017).
30. Pachitariu, M. & Stringer, C. Cellpose 2.0: how to train your own model. *Nat. Methods* **19**, 1634–1641 (2022).
31. Garlick, E., Thomas, S. G. & Owen, D. M. Super-Resolution Imaging Approaches for Quantifying F-Actin in Immune Cells. *Front Cell Dev. Biol.* **9**, 676066 (2021).
32. Fritzsche, M. et al. Cytoskeletal actin dynamics shape a ramifying actin network underpinning immunological synapse formation. *Sci. Adv.* **3**, e1603032 (2017).
33. Mestermann, K. et al. The tyrosine kinase inhibitor dasatinib acts as a pharmacologic on/off switch for CAR T cells. *Sci. Transl. Med.* **11**, 5907 (2019).
34. Tong, C. et al. Optimized tandem CD19/CD20 CAR-engineered T cells in refractory/relapsed B-cell lymphoma. *Blood* **136**, 1632–1644 (2020).
35. Liu, D. et al. The Role of Immunological Synapse in Predicting the Efficacy of Chimeric Antigen Receptor (CAR) Immunotherapy. *Cell Commun. Signal.* **18**, 1–20 (2020).
36. Yi, J., Wu, X. S., Crites, T. & Hammer, J. A. Actin retrograde flow and actomyosin II arc contraction drive receptor cluster dynamics at the immunological synapse in Jurkat T cells. *Mol. Biol. Cell* **23**, 834–852 (2012).
37. Matalon, O. et al. Actin retrograde flow controls natural killer cell response by regulating the conformation state of SHP-1. *EMBO J.* **37**, e96264 (2018).
38. Tamzalit, F. et al. Centrioles control the capacity, but not the specificity, of cytotoxic T cell killing. *Proc. Natl Acad. Sci. USA* **117**, 4310–4319 (2020).
39. Shi, Y. et al. Smart lattice light-sheet microscopy for imaging rare and complex cellular events. *Nat. Methods* **21**, 301–310 (2024).
40. Simonyan, K. & Zisserman, A. Very deep convolutional networks for large-scale image recognition. *arXiv* **1409**, 1556 (2015).
41. Liang, L., Jin, Y. X., Zhu, X. Q., Zhou, F. L. & Yang, Y. Real-time detection and monitoring of the drug resistance of single myeloid leukemia cells by diffused total internal reflection. *Lab Chip* **18**, 1422–1429 (2018).
42. Wang, N. et al. Efficacy and safety of CAR19/22 T-cell cocktail therapy in patients with refractory/relapsed B-cell malignancies. *Blood* **2**, 17–27 (2020).
43. Lukinavicius, G. et al. Fluorogenic probes for live-cell imaging of the cytoskeleton. *Nat. Methods* **11**, 731–733 (2014).
44. Zhu, T. et al. Large-scale high-throughput 3D culture, imaging, and analysis of cell spheroids using microchip-enhanced light-sheet microscopy. *Biomed. Opt. Express* **14**, 1659–1669 (2023).
45. Weigert et al. Content-aware image restoration: pushing the limits of fluorescence microscopy. *Nat. Methods* **15**, 1090–1097 (2018).
46. Wolny, A. et al. Accurate and versatile 3D segmentation of plant tissues at cellular resolution. *Elife* **9**, 1–34 (2020).
47. Arzt, M. et al. LABKIT: Labeling and Segmentation Toolkit for Big Image Data. *Front. Comput. Sci.* **4**, 777728 (2022).

Acknowledgements

The authors would like to thank Dr. Meng Zhang, Prof. Yuhui Zhang, and Prof. Liang Huang for providing us insightful biomedical supports, thank Optoelectronic Micro&Nano Fabrication and Characterizing Facility of Huazhong University of Science and Technology for providing technical support on photolithography technology. This work was supported by

the funding from National Natural Science Foundation of China (T2225014, 82270238, 21927802). National Key Research and Development Program of China (2022YFC3401102). Figure 1c, created with BioRender.com, released under a Creative Commons Attribution-NonCommercial-NoDerivs 4.0 International license.

Author contributions

P.F., Li.C. and Z.W. conceived the idea. P.F. and Li.C. oversaw the project. J.J., M.Z. and S.M. conducted the cell experiments. Y. Zhao., J. W. and Y. Zhou. developed the optical setups and acquired the experimental images. Z.W., W.S., Lo.C. developed the programs and processed the images. P.F., Lo.C., Z.W., W.S. and J.J. analyzed the data. Z.W., J.W., Li.C., Y.Zhang., C.Z. and P.F. discussed and wrote the paper.

Competing interests

The authors declare no competing interests.

Additional information

Supplementary information The online version contains supplementary material available at <https://doi.org/10.1038/s41467-024-51039-9>.

Correspondence and requests for materials should be addressed to Liting Chen or Peng Fei.

Peer review information *Nature Communications* thanks Qionghai Dai, Michael Dustin, Reto Fiolka and the other, anonymous, reviewer(s) for

their contribution to the peer review of this work. A peer review file is available.

Reprints and permissions information is available at <http://www.nature.com/reprints>

Publisher's note Springer Nature remains neutral with regard to jurisdictional claims in published maps and institutional affiliations.

Open Access This article is licensed under a Creative Commons Attribution-NonCommercial-NoDerivatives 4.0 International License, which permits any non-commercial use, sharing, distribution and reproduction in any medium or format, as long as you give appropriate credit to the original author(s) and the source, provide a link to the Creative Commons licence, and indicate if you modified the licensed material. You do not have permission under this licence to share adapted material derived from this article or parts of it. The images or other third party material in this article are included in the article's Creative Commons licence, unless indicated otherwise in a credit line to the material. If material is not included in the article's Creative Commons licence and your intended use is not permitted by statutory regulation or exceeds the permitted use, you will need to obtain permission directly from the copyright holder. To view a copy of this licence, visit <http://creativecommons.org/licenses/by-nc-nd/4.0/>.

© The Author(s) 2024